

SCIENTIFIC REPORTS

OPEN

Chitosan coated cotton cloth supported zero-valent nanoparticles: Simple but economically viable, efficient and easily retrievable catalysts

Fayaz Ali^{1,2}, Sher Bahadar Khan^{1,2}, Tahseen Kamal^{1,2}, Khalid A. Alamry², Abdullah M. Asiri^{1,2} & Tariq R. A. Sobahi²

A simple, economically viable and fast method has been utilized for the preparation of highly active metal nanoparticles (MNPs) in coating layer of chitosan (CH) over cellulose microfibers of cotton cloth (CC). 2 wt% of CH solution was used for the coating of CC strips (CC-CH), and were kept in aqueous solutions of metal salts to adsorb metal ions. The CC-CH templated with metal ions were then treated with aqueous solution of NaBH_4 to reduce the metal ions into zero-valent metal nanoparticles (M^0). The CC-CH strips loaded with M^0 were characterized by XRD, XPS, ATR-FTIR, FE-SEM and TGA, which indicates the successful synthesis of MNPs by this method. The $\text{M}^0/\text{CC-CH}$ strips were used as an efficient catalyst for the model reduction reaction of nitrophenol and toxic organic dyes. Among all the prepared samples, Fe/CC-CH showed good catalytic activity for 4-NP and Rh-B dye reduction in the presence of NaBH_4 with rate constants of 0.2937 min^{-1} and 0.3804 min^{-1} , respectively. Moreover Fe/CC-CH has good catalytic reduction ability for MO and MB having rate constants equal to 0.1698 and 0.2802 min^{-1} , respectively. Beside the good catalytic ability, it could be easily recoverable as compared to other available techniques. The recovery was completed by simply pulling the strip from the reaction matrix after completion of the reaction and can be used several times.

In recent years, the development of new catalytic system for the conversion of toxic chemicals into fine chemicals has become a foremost research area. The rational design of active, durable and selective catalysts is essential which can be tested on hazardous chemicals conversion. The use of catalyst in liquid phase can aid substantially in the recovery, separation and reuse of catalyst and also required afford for product separation from reaction matrix, thus major contribution on the synthetic procedure is required for environmental performance.

Recently, metallic nanoparticles (MNPs) have attracted much attention from the researchers community because of their various applications in variety of fields, *i.e.* sensing, bio-sensing, antimicrobial coating, drug delivery and so-on. Beside these common applications, MNPs are extensively applied as catalysts in various chemical reactions such as Suzuki-cross-coupling¹, hydrogen liberation², hydrocarbon oxidation^{3,4}, phenolic derivative upgradation reactions⁵ and ring opening⁶. MNPs have high activity due to their small sizes which originates from their high surface to volume ratio. Most of the MNPs can removed different pollutants due to their electron donating tendency including the anions through reduction. Due to these properties, a considerable attention of the environmental researchers has been attracted towards the metal nanoparticles⁷⁻⁹. Therefore, most of MNPs applied for removal of toxic chemicals including: Fe, Cu, Co, Ag, Ni, Ti, Pd, Pt and Al^{8,10,11}. Two main hurdles are associated with the practice of MNPs as a catalyst. Firstly, agglomeration of nanoparticles readily occurs due to van der Waals forces, and prevention of these agglomerate is difficult. Such agglomeration of nanoparticles drops the catalytic activity because it results in decrease of surface area¹². Secondly, the separation of nanoparticle is difficult after completion of reactions because of their small size¹³. Researcher focused their efforts to overcome

¹Center of Excellence for Advanced Materials Research, King Abdulaziz University, P.O. Box 80203, Jeddah, 21589, Saudi Arabia. ²Department of Chemistry, King Abdulaziz University, P.O. Box 80203, Jeddah, 21589, Saudi Arabia. Correspondence and requests for materials should be addressed to S.B.K. (email: sbkhan@kau.edu.sa)

the above-mentioned hurdles. They suggested that the single solution was to utilize catalytic supports to prevent agglomeration and easy recycling of nanoparticles. The usage of catalyst support has two-fold benefits. Firstly, they improve the dispersability and stability and secondly, the separation and reuse of catalyst from the reaction matrix become easy^{14,15}. Nanoparticles can be assembled or supported on high surface area materials, and the resulting composite materials can be used as a catalyst for model reaction.

Cotton cloth (CC) is well known porous and flexible fabric made from natural cotton fibers, which has high porosity and hierarchical network structure with functional groups such as hydroxyl groups forming complicated surface morphology^{16,17}. For instance, each cotton fiber is composed of multiple individual cotton fibrils, which are in turn composed of multiple micro-fibrils bundled together^{16,18}. The micro-fibrils are made of poly-D-glucose chains, which are usually arranged in partially crystalline domains¹⁶. This structure allows the fiber to absorb large amounts of water and other polar solvents, which causes the cotton fibers to swell when placed in a solution.

Chitosan (CH) is a polysaccharide which is derived from the deacetylation of chitin. Chitin is abundantly available in nature and commonly found in many invertebrates and in the cell wall of most algae and fungi¹⁹. The physical, chemical and functional characteristics make it to be considered as an incredible and versatile polymer. The advantageous properties of CH include its biodegradability, biocompatibility, cationic nature, good adsorption capacity, film-forming capabilities, adhesive characteristics, permeability-enhancing effect and many more, and is considered as cost-effective and safe^{20,21}. However, it is often dissolved in acidic medium because it's not completely soluble in water and thus limit its application in various fields. Despite of its solubility shortcomings, it has been applied in various fields and in many industries, such as; biotechnology, medical, pharmaceuticals, cosmetic, food and nutrition, water engineering, ophthalmology, paper technology, photography and others^{20,22,23}. The availability of free amino groups in its structure provide various modification possibilities which can be further functionalized to increase capacity for metal ions uptake^{24–27}.

From the past few years, synthetic polymer-based catalyst supports were synthesized, and catalytic efficiencies of various metal nanoparticles were analyzed^{25,28,29}. The hydrogels were exposed as good supports for catalyst in aquatic chemical reactions because in this case the catalyst surface is exposed to the reactant molecules^{30,31}. However, hydrogels are soft and break during handling. Therefore, to avoid the long procedure for the designing and preparation of new materials, we relied on abundantly available natural resources such as cotton^{17,18} and CH (derivative of chitin)^{29,32} as catalytic support.

Herein, we present a facile and cost-effective method to synthesize MNPs on CC-CH as a catalyst for water treatment. The $M^0/CC-CH$ were made by CH aqueous solution coating on CC, adsorption of metal ions (M^+) from their respective aqueous salt solutions followed by treating the samples with $NaBH_4$ solution to convert M^+ to their respective zero-valent metal nanoparticles (M^0). The synthesized samples were characterized by using FT-IR, XRD, XPS, TGA and FE-SEM. The $M^0/CC-CH$ were applied as dip-catalysts in chemical reduction of nitrophenols and azo dyes. These azo dyes and nitrophenols are highly toxic and many struggles have been made which exploited the proficient catalysts to transform them into non-toxic substances. The nano-zero-valent iron (Fe) nanoparticles loaded on CC-CH exhibited high catalytic efficiency for the conversion of these toxic substances. This novel Fe/CC-CH has great potential to apply as an environmentally friendly, economical, easily recyclable and sustainable catalyst.

Experimental

Materials. Chitosan in the form of yellowish powder with a degree of deacetylation >75% and high molecular weight was purchased from Sigma-Aldrich, Ireland. Sodium borohydride ($NaBH_4$, 99%), acetic acid, ferrous sulphate heptahydrate ($FeSO_4 \cdot 7H_2O$, 98%), nickel sulphate heptahydrate ($NiSO_4 \cdot 7H_2O$, 99%), copper sulphate pentahydrate ($CuSO_4 \cdot 5H_2O$, 98.5%), cobalt chloride hexahydrate ($CoCl_2 \cdot 6H_2O$), 4-nitrophenol (4-NP) and 2-nitrophenol (2-NP) were purchased from BDH chemicals, England. Silver nitrate ($AgNO_3$) was purchased from MERCK. Rhodamine-B (Rh-B), methylene blue (MB) and methyl orange (MO) dyes were purchased from Koch-lite laboratories, England. All chemicals were of analytical grade and utilized without any further purification. This work was carried out with water having resistivity of 18.2 M Ω cm.

Catalyst synthesis. The following procedure of two-steps was implemented for the synthesis of catalyst

1. The yellowish chitosan (CH) solution was prepared by dissolving 2% w/v of CH in dilute acetic acid aqueous solution (20%v/v) by stirring overnight at room temperature. It was then coated on cotton cloth (CC) by dipping the rectangular pieces ($0.4 \times 2 \text{ cm}^2$) of CC in this solution for 10 min. The excess solution was wiped out from the pieces of CC and kept for drying.
2. MNPs were synthesized inside CH layer on CC by adsorption of metal ions followed by their reduction with $NaBH_4$. As mentioned above that pieces of CC were treated with CH solution to form CC-CH strips. Then CC-CH strips were kept in separate aqueous solutions of metal salts of $FeSO_4 \cdot 7H_2O$, $NiSO_4 \cdot 7H_2O$, $CuSO_4 \cdot 5H_2O$, $CoCl_2 \cdot 6H_2O$ and $AgNO_3$ for 4 hours, which turned the white CC-CH strips to yellowish, greenish, irish blueish, reddish and brownish respectively. The strips were then gently washed with deionized water, and introduced into 100 mL of 0.1 M $NaBH_4$ aqueous solution. The black color was observed as soon as these strips were introduced into $NaBH_4$ aqueous solution. The strips were remaining dipped for 30 min in $NaBH_4$ solution to completely reduce the metal ions into zero-valent metal nanoparticles (M^0). The strips of CC-CH loaded with MNPs ($M^0/CC-CH$) were washed with deionized water after this step, and freshly used in further analysis.

Characterization. Crystal structure of the samples were analyzed by using X-ray diffraction (XRD) on PANalytical diffractometer with a Cu $K\alpha$ radiations ($\lambda = 0.154 \text{ nm}$) source. The XRD was operated at 40 KV and

50 mA, and data were recorded at a scan rate of $2^\circ 2\theta \text{ min}^{-1}$. The crystallinity percentage (Cr%) were calculated from the XRD patterns of pure CC, CC-CH, and MNPs loaded on CC-CH samples, using the following equation (1),

$$\text{Cr\%} = \frac{I_{(200)} - I_{\text{amorphous}}}{I_{(200)}} \times 100 \quad (1)$$

where $I_{\text{amorphous}}$ and $I_{(200)}$ represent the intensity of the amorphous halo and the intensity of the (200) peak, respectively. For the cellulose I, the at $2\theta = 18^\circ$ in the diffraction pattern was chosen as $I_{\text{amorphous}}$. Crystallite size of the loaded MNPs were calculated using scherrer equation as given below in Eq. (2),

$$\tau = \frac{K\lambda}{\beta \cos\theta} \quad (2)$$

where τ is the crystallite size, λ wavelength of X-rays, β full width of the peak at half minimum (FWHM) and θ is the scattering angle of the peak. XRD patterns were analyzed by Fityk software to calculate the FWHM values from the XRD patterns. Fourier transform infrared (FTIR) spectra of the samples were recorded in the range of $700\text{--}4000 \text{ cm}^{-1}$ using PerkinElmer (spectrum100) ATR-FTIR spectrometer. X-ray photoelectron spectroscopy (XPS) Thermo Scientific K-Alpha KA1066 spectrometer (Germany) in the range of 200 to 1350 eV was investigated for the elemental analysis as well as for the determination of binding energy in the respective catalyst. The morphology of the samples was examined by field emission scanning electron microscope (FESEM) with a JEOL JSM-7600F, Japan. Energy dispersive X-ray spectrometry (EDS) of the samples was performed for the elemental analysis by using the Oxford-EDS system. Thermogravimetric analysis of 10 mg sample was performed by using TGA Q500 instrument. The samples were put in the aluminum pans and the autosampler stage of the instrument was kept on. Their weight lost against temperature under nitrogen atmosphere was recorded with a heating rate of $10^\circ\text{C}/\text{min}$ upto 700°C . The residual concentration of nitrophenol and azo dyes was monitored and recorded by using Thermo scientific, Evolution 300 UV-visible spectrophotometer.

Evaluation of catalytic activity. The catalytic activities of $\text{M}^0/\text{CC-CH}$ was evaluated in the reduction of nitrophenol (4-NP) and azo dye (Rh-B) by NaBH_4 . We used quartz UV cuvette cell as reaction vessel. We prepared three solutions of NaBH_4 , 4-NP and Rh-B with concentration of 0.1 M, 0.1 mM and 0.05 mM respectively, in DI water. As an example, we explain the typical procedure adopted for the conversion of 4-nitrophenol to 4-aminophenol by NaBH_4 using the prepared catalyst. To UV cuvette, 3 mL of 4-NP and 0.5 mL of NaBH_4 solution were added, and place in UV-visible spectrophotometer to record the UV-visible spectra. After this, the $\text{M}^0/\text{CC-CH}$ strip was added to this cuvette in such a way that UV-visible light can easily pass through it. The reduction reaction was started as soon as the catalytic strip was added and continuously recorded the absorption spectra. The recorded variation in the absorbance value of 4-NP at 400 nm was plotted and compared with the calibration curve. The catalytic strip was easily removed from the reaction vessel by just pulling the strip from cuvette and used it again for 4-NP conversion. The recyclability of the catalyst was performed after washing the catalytic strip with DI water and used again for 4-NP conversion reaction. The same procedure was implemented for the reduction reaction of Rh-B dye.

For sake of comparison, the catalytic activity of the bare CC and CC-CH was also tested. The catalytic efficiency of $\text{Fe}/\text{CC-CH}$ for 4-NP and Rh-B was high as compared to other loaded MNPs, therefore we also investigated its activity towards other dyes like MB and MO. The concentration of these dyes was 0.05 mM. In all reaction, we used fresh catalytic strips except the recyclability experiments where same strip was used.

Results and Discussion

Figure 1 shows the steps involved in the preparation of $\text{M}^0/\text{CC-CH}$ catalytic strips. CC coating by CH resulted in mechanically strong and slightly brittle CC-CH as compare to the pure CC because the individual cellulose microfibers was connected by CH polymer. Then color of the CC-CH strips was change from white to yellowish, irish blueish, reddish, brownish and greenish after treating with aqueous solution of metal salt Fe, Cu, Co, Ag and Ni, respectively. The color change confirmed the uptake of metal ions by $-\text{NH}_2$ and $-\text{OH}$ groups present in CH layers of CC-CH strips. The formation of M^0 was carried out by dipping the CC-CH loaded with metal ions in the aqueous solution of NaBH_4 followed by color change to black. The color change took just few seconds, which indicates that the reaction of NaBH_4 with metal ions was quite fast. The chemical reactions during this process are proposed as follow in Eq. (3–7):



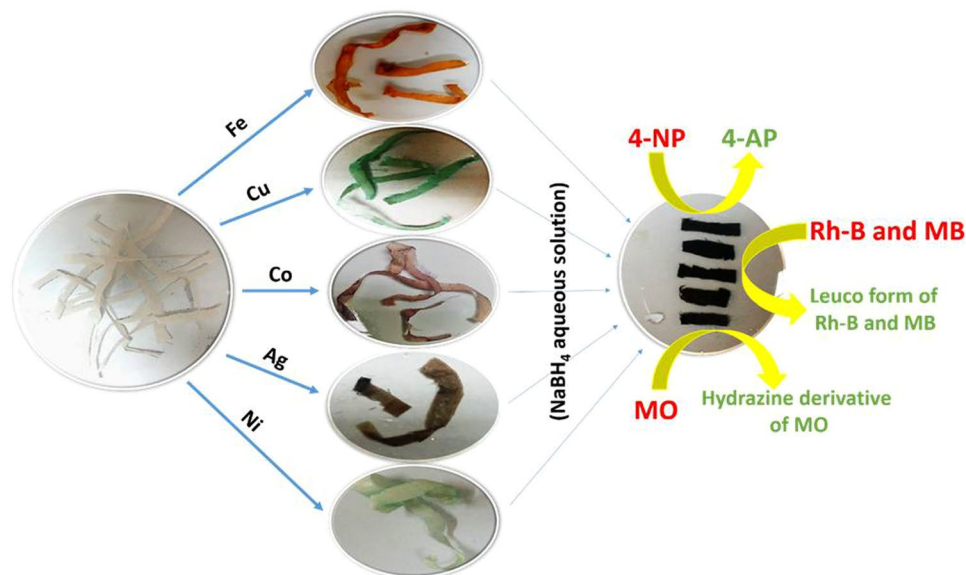


Figure 1. CC-CH pieces treated with Fe, Cu, Co, Ag and Ni salt aqueous solution, separately treated with NaBH_4 aqueous solution after cutting in small equal strips and then these strips applied as catalyst for catalytic reduction of 4-NP, Rh-B, MB and MO solutions.

The successful synthesis of Co^0 , Cu^0 , Ag^0 , Ni^0 and Fe^0 nanoparticles depends on the water quality. In previous reports, water in NaBH_4 aqueous solution was deoxygenated by using nitrogen or other inert gases to avoid metal oxide formation^{33,34}. The M^0 were also protected from their oxidation by the hydrogen gas release in the above reaction⁷. However, we used freshly prepared DI water for NaBH_4 solution, where chances for dissolved oxygen was low. The prepared CC-CH strips loaded with different M^0 were then tested in the reduction reactions of nitrophenol and dyes solutions.

Crystal structure and morphology. *XRD.* Figure 2 shows the XRD patterns of the bare CC, and the loaded CC-CH with Fe, Cu, Ag, Co and Ni nanoparticles. All the patterns have diffraction peaks at 14.9° , 16.7° , 22.9° and 34.7° can be observed which correspond to (110), (110), (200) and (004) planes of cellulose I. The XRD pattern of the loaded CC-CH with Fe, Cu, Ag, Co and Ni were identical to the bare CC, which suggest that crystalline cellulose content was present in all samples and CH was only amorphously adsorbed on the CC. The crystallinity of all the samples were in the range of 70 to 77%, and the crystallite size was about 6.92 to 7.03 nm. The cellulose crystallinity and crystallite size of the MNPs loaded CC-CH were almost similar to the bare CC. These observations manifested that cellulose reserved its structure after processing with CH for the preparation of MNPs, which is of intense need for its mechanical properties. In addition to amorphous and crystalline peaks of cellulose fibers of CC, the sharpest peak of Fe nanoparticles was also observed at $2\theta = 43.7^\circ$, corresponding to (400) plane of Fe nanoparticles according to JCPDS no 98-000-0064, which is in line with other reported literature³⁵. Cu nanoparticles has a sharpest peak at $2\theta = 43.72^\circ$ corresponding to (111) reflection, according to the JCPDS card # 04-0836, which can be observed in the XRD pattern of Cu/CC-CH. Similarly, in the XRD pattern of Ag/CC-CH, we can observe the peaks at $2\theta = 38$ and 43.8° , corresponding to the (111) and (200) reflection planes and were in good agreement with previous reports^{36,37}. Moreover, according to JCPDS, card no 15-0806, Co nanoparticles has a diffraction peak at 43.8° corresponding to (111) crystal plane, which was observed here in Co/CC-CH indicating the preparation of cubic crystalline cobalt. Actually two modification of Co coexist at room temperature, which is face-center cubic (FCC) and hexagonal close-packed (HCP), and are often difficult to separate³⁸. Here, the prepared Co nanoparticles were determined to be FCC by JCPDS database, since in the reported pattern the FCC crystal structure was dominant. Also, no cobalt oxide or carbide phase was observed in the reported pattern, since their peaks are at $2\theta = 42.4^\circ$ (JCPDS card no. 09-0402) and 47.57° (JCPDS card no. 05-0727), respectively. In the Ni/CC-CH diffraction pattern, the peak at $2\theta = 44^\circ$ confirms the presence Ni nanoparticles of (111) plane (according to JCPDS file no. 04-0850), in addition to the cellulose peaks. Since, in all XRD patterns of MNPs loaded on CC-CH, no other peaks related to their oxide or hydroxide was observed, which suggest the successful synthesis of zero-valent MNPs in the layers of CH on CC.

FTIR. Figure 3a,b shows the FTIR spectra of all the samples (bare CC and CC-CH and loaded with MNPs) recorded in the range between 700 cm^{-1} and 4000 cm^{-1} . This figure suggests that all the other spectra were identical to those of pure CC spectrum. All the spectra exhibited a typical cellulose FTIR, which was widely described in previous literature^{39,40}. Also, its peaks at are well assigned and discussed in previous reports^{41,42}. FTIR analysis suggests that no interaction occur between oxygenated functional groups of CC, CH amino and oxygenated groups, and MNPs because in all spectra the peaks were located on the same position. The interaction of CH and MNPs with CC in low extent might be due to low content of CH and MNPs in the samples.

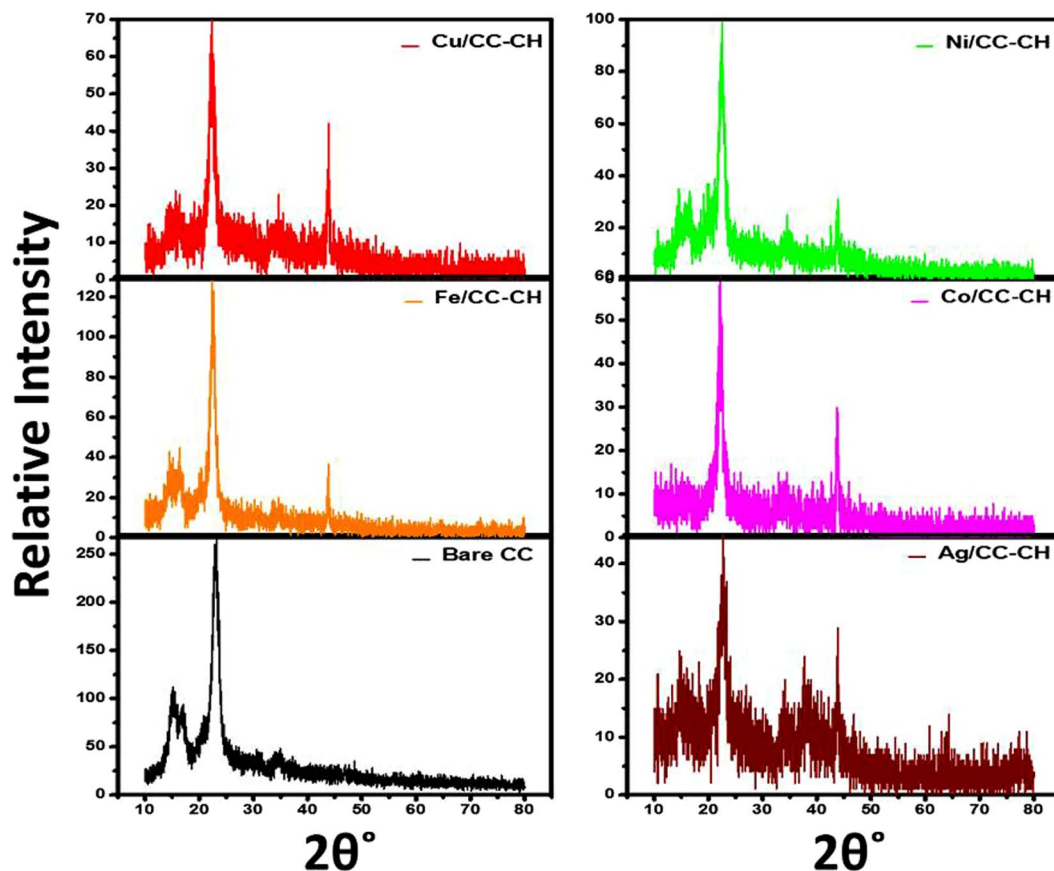


Figure 2. XRD patterns of bare CC and loaded CC-CH with Fe, Cu, Ag, Co and Ni nanoparticles.

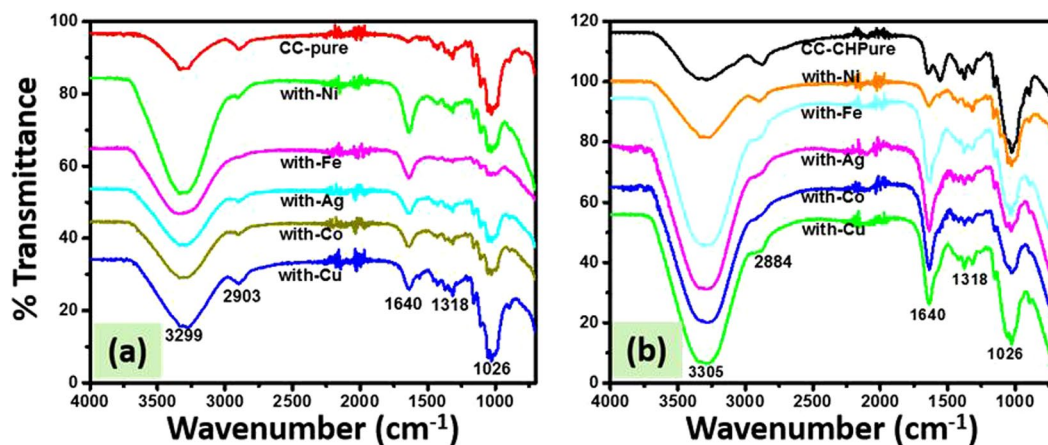


Figure 3. FTIR spectra of bare CC and loaded with Ni, Fe, Ag, Co and Cu nanoparticles (a), and bare CC-CH and loaded with Ni, Fe, Ag, Co and Cu nanoparticles (b).

XPS. The XPS analysis of MNPs located on CC-CH surface in comparison with unloaded CC-CH is manifested in Fig. 4a–e. The valence state of the metals on the CC-CH surface is in the reduced form. For instance, Fig. 4a shows the XPS Cu $2p_{3/2}$ survey, presenting a photoelectron peak, this peak is selected to the chemically reduced Cu^0 , based on the additional Auger line survey. However, for the survey of Co/CC-CH, our XPS analysis did not confirm that loaded Co nanoparticles were present in their zero-valent form. Referring to this analysis, the recorded Co $2p_{3/2}$ peaks were positioned at 781 ± 0.3 eV and towards the high binding energy side. This value happens in between the earlier reported values corresponding to Co^{2+} in $\text{Co}(\text{OH})_2$ (782 ± 0.1 eV for the $2p_{3/2}$ line)⁴³ and to Co^{2+} in CoO (780 ± 0.2 eV for the $2p_{3/2}$ line)⁴⁴. This line is very closer to the corresponding metallic cobalt, Co^0 (778 ± 0.2 eV for the Co $2p_{3/2}$ line)⁴⁵. Based on this, it could be proposed that Co^{2+} ions were simply precipitated on surface of CC-CH in the form of $\text{Co}(\text{OH})_2$ or fixed by the hydroxyl groups at that surface. Nevertheless, the XPS survey of Ag $3d_{5/2}$, has exposed only

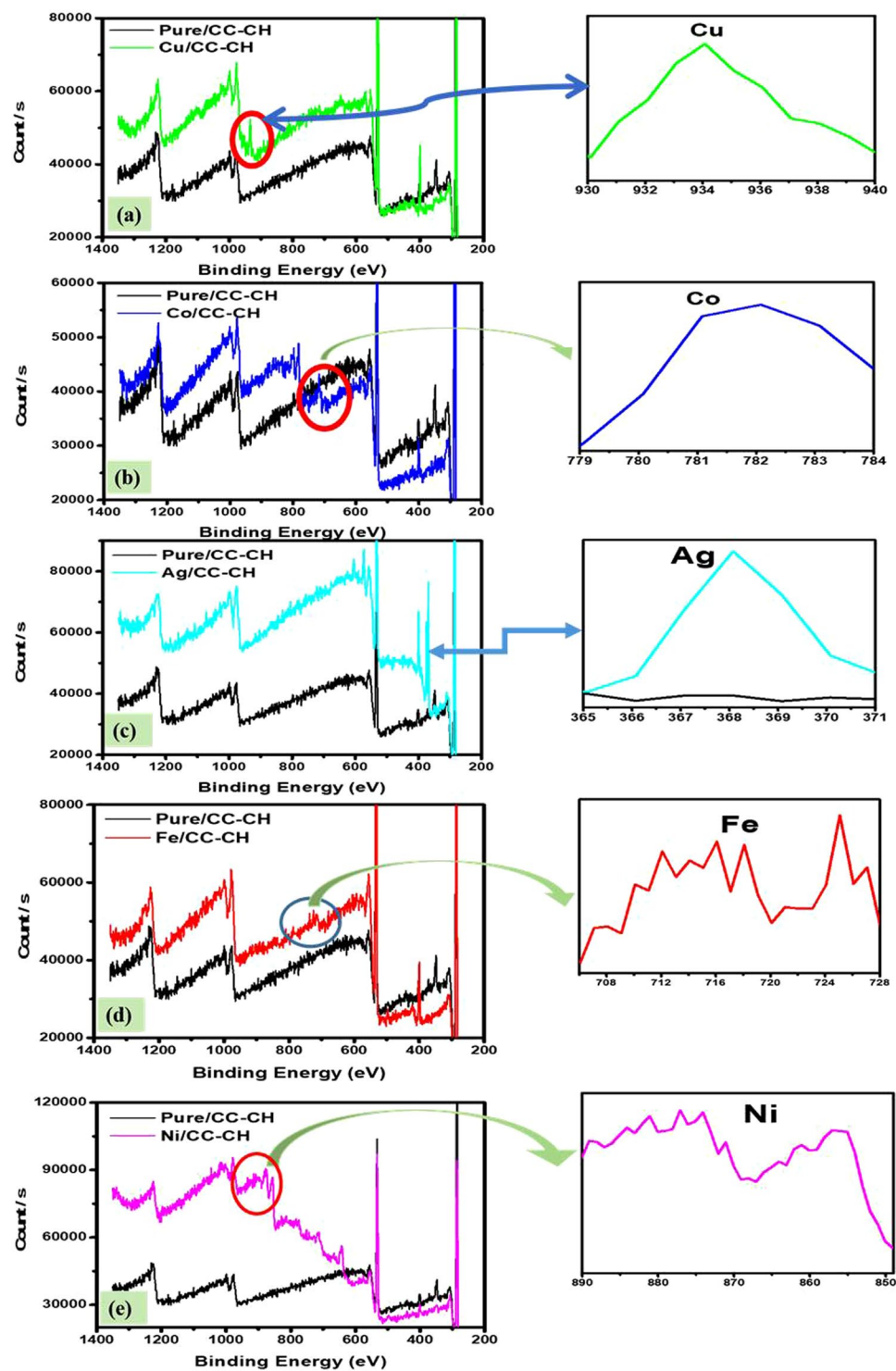


Figure 4. Comparison of XPS wide-scan survey of bare CC-CH and CC-CH coated with Cu (a), Co (b), Ag (c), Fe (d) and Ni (e) nanoparticles and their high resolution, respectively.

one valence state on the surface, which represent the reduced MNP, i.e., Ag^0 (Fig. 4c). Thus, Ag^0 nanoparticles are reserved on the CC-CH surface by chemical reduction and precipitation. For the survey of Fe 2p core levels (Fig. 4d), the photoelectron peaks at 711 eV, 719 eV and 725 eV epitomize the binding energies of Fe($2p_{3/2}$), shake-up satellite $2p_{3/2}$ and $2p_{1/2}$, respectively. These three main peaks of Fe suggest that the surface CC-CH strip mainly consist of iron nanoparticles^{46,47}. Furthermore, a small shoulder at around 706.98 eV suggesting the $2p_{3/2}$ peaks of zero-valent iron (Fe^0). The Ni $2p_{3/2}$ survey offers a small shoulder peak at 852 and another peak at 855 eV. That is, both Ni^0 (852 eV) and Ni(II) (855 eV) are present on the CC-CH surface⁴⁷. The presence of both the zero-valent and their oxidized form of nanoparticles might be due to exposure for long time to air atmosphere during XPS analysis.

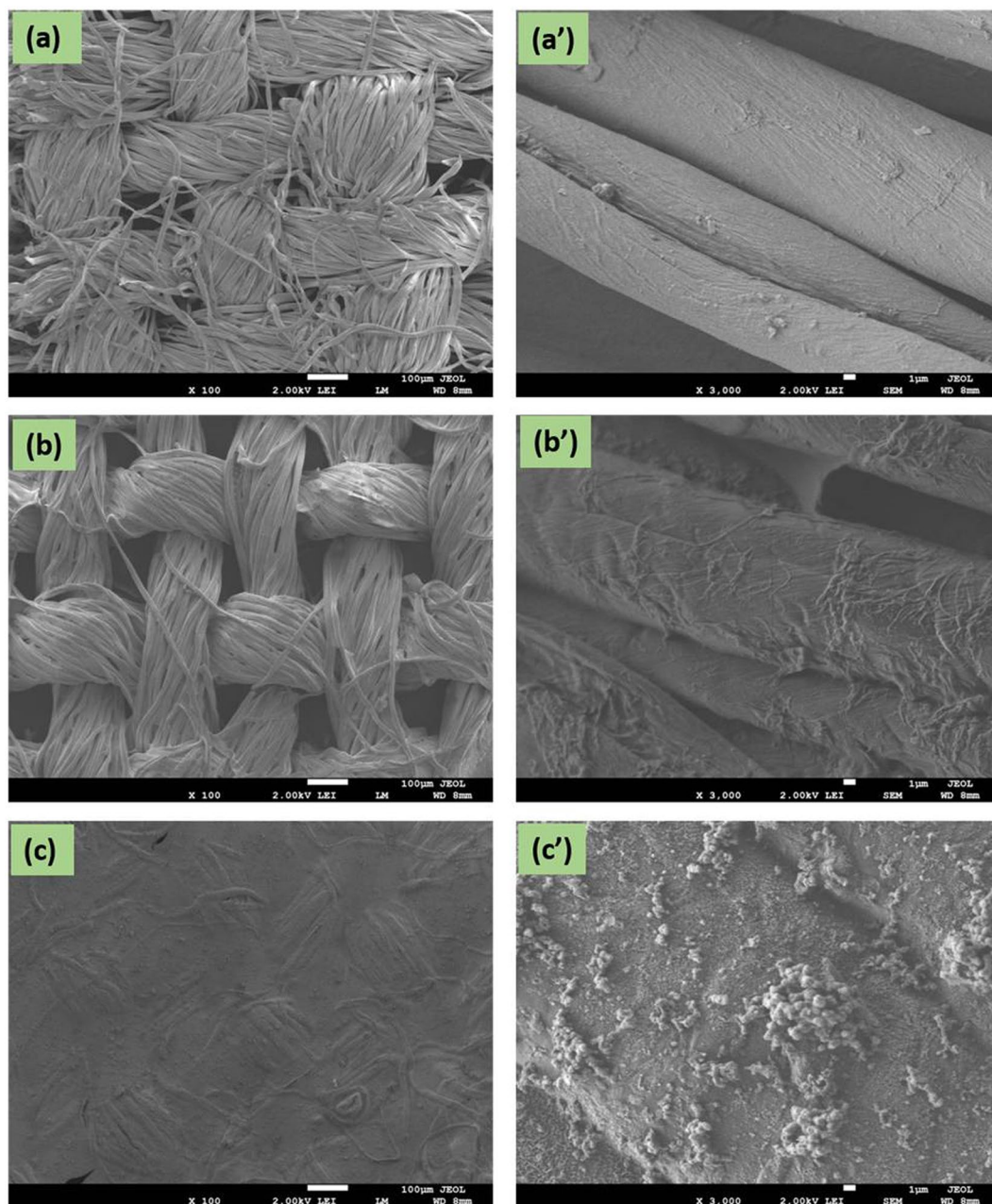


Figure 5. FE-SEM image of CC (a), CC-CH (b) and Fe/CC-CH (c) of low magnification and their respective high magnification (a'–c').

FE-SEM and EDX. We used FE-SEM to analyze the morphologies of CC, CC-CH and Fe/CC-CH. Figure 5a–c exhibits the SEM images of all the samples. The left side images in (a–c) low magnification and the right side (a'–c') exhibits high magnification. The FE-SEM image of CC was composed of microfibers as manifested in (Fig. 5a). The original morphology of CC upon treating with 5 wt% CH solution did not change (Fig. 5b). CC-CH was morphologically identical to the untreated CC and there were micropores in it. Initially, individual microfibers of CC are covered by a thin CH layer, as reveals by the images in (aa') and (bb'). The CH thin layer are partly connecting the fibers, however, some of the fibers are separated from each other, which pointing to the fact that this layer might be wrapping these fibers. This result suggests that CH was adsorbed in the form of thin layer around the CC microfibers. In case of Fe/CC-CH, a significant morphological changes can be observed at micrometer scale. From Fig. 5c plenty of small spots can be observed on microfibers, which indicate that Fe nanoparticles have been successfully formed on the surface of CC-CH, as already confirmed by XRD analysis. Some aggregates were also observed in the SEM image at high resolution (Fig. 5c'). Beside some aggregation most of the CC fibers surface was covered with well separated and uniform Fe nanoparticles. The successful synthesis of Fe nanoparticles on CH layer over CC microfibers was also confirmed by EDS analysis (Fig. 6a–c). The elemental Fe can be clearly observed in the EDX spectrum of Fe/CC-CH (Fig. 6c). Other elements carbon and oxygen observed in EDS analysis were mostly due to the presence of various functional groups in CC and CH.

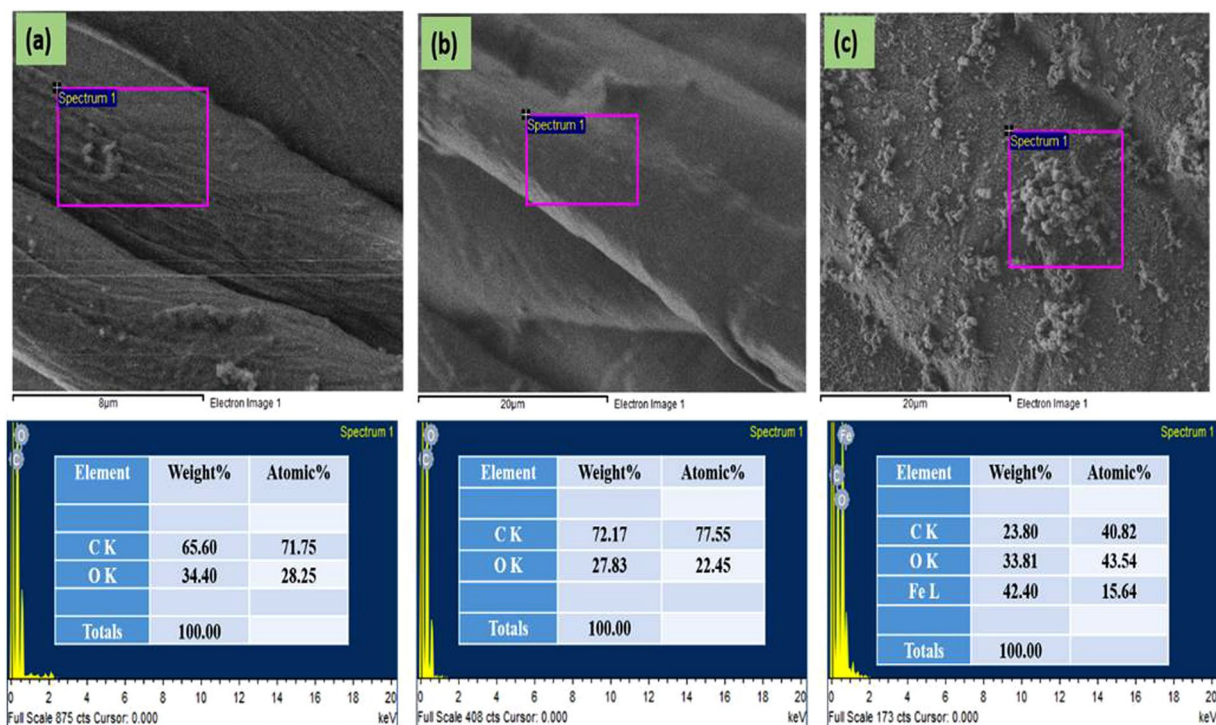


Figure 6. EDX spectra of CC (a), CC-CH (b) and Fe/CC-CH (c).

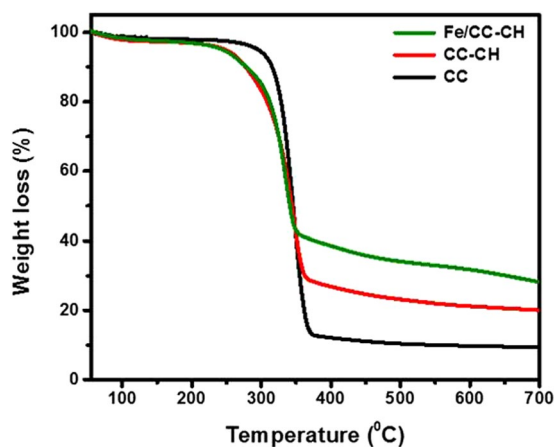


Figure 7. TGA thermogram of CC, CC-CH and Fe/CC-CH.

TGA. TGA thermograms of CC, CC-CH and Fe/CC-CH were elaborated in Fig. 7. All the sample lost around 10% of their original weight while increasing the temperature to 100 °C. The initial weight loss was due to the abolition of moisture from the samples. Moreover, an apparent and huge weight loss can be observed between 260 °C and 360 °C. This reduction of weight was due to oxidation, depolymerization and evolution of gases from cellulose and CH main organic portions. In contrast to other reports on addition of nanomaterial to polymer matrices, which increases the degradation temperature of polymer, a lowering in thermal stability of Fe/CC-CH was observed, which might be due to the catalytic nature of Fe nanoparticles. Usually nanoparticles increase the depolymerization and decreases the activation energy during thermal process^{29,48,49}. Thermal decomposition temperature data obtained from TGA spectrum of CC, CC-CH and Fe/CC-CH are manifested in Table 1. In this table, (T_{onset}) is the initiation of the thermal decomposition temperature at which cellulose microfibers start to decompose, (T_{max}) is the maximum degradation rate temperature and (T_{end}) is the decomposition end temperature. From Table 1, it is clear that T_{onset} , T_{max} and T_{end} were slightly lower for Fe/CC-CH and CC-CH than CC. Another objective of TGA analysis was to determine the amount of Fe nanoparticles in Fe/CC-CH strip. The difference between Fe/CC-CH and CC-CH thermogram at 700 °C at 7.77%, which suggest that the strip of almost 10 mg of Fe/CC-CH contain 0.7 ± 0.5 mg of Fe nanoparticles.

Samples	T _{onset} (°C)	T _{max} (°C)	T _{end} (°C)	Weight loss (%) at 700 °C
CC	229	339	371	9.48
CC-CH	194	334	362	20.40
Fe/CC-CH	190	325	351	28.17

Table 1. Important parameters calculated from TGA analysis of CC, CC-CH and Fe/CC-CH.

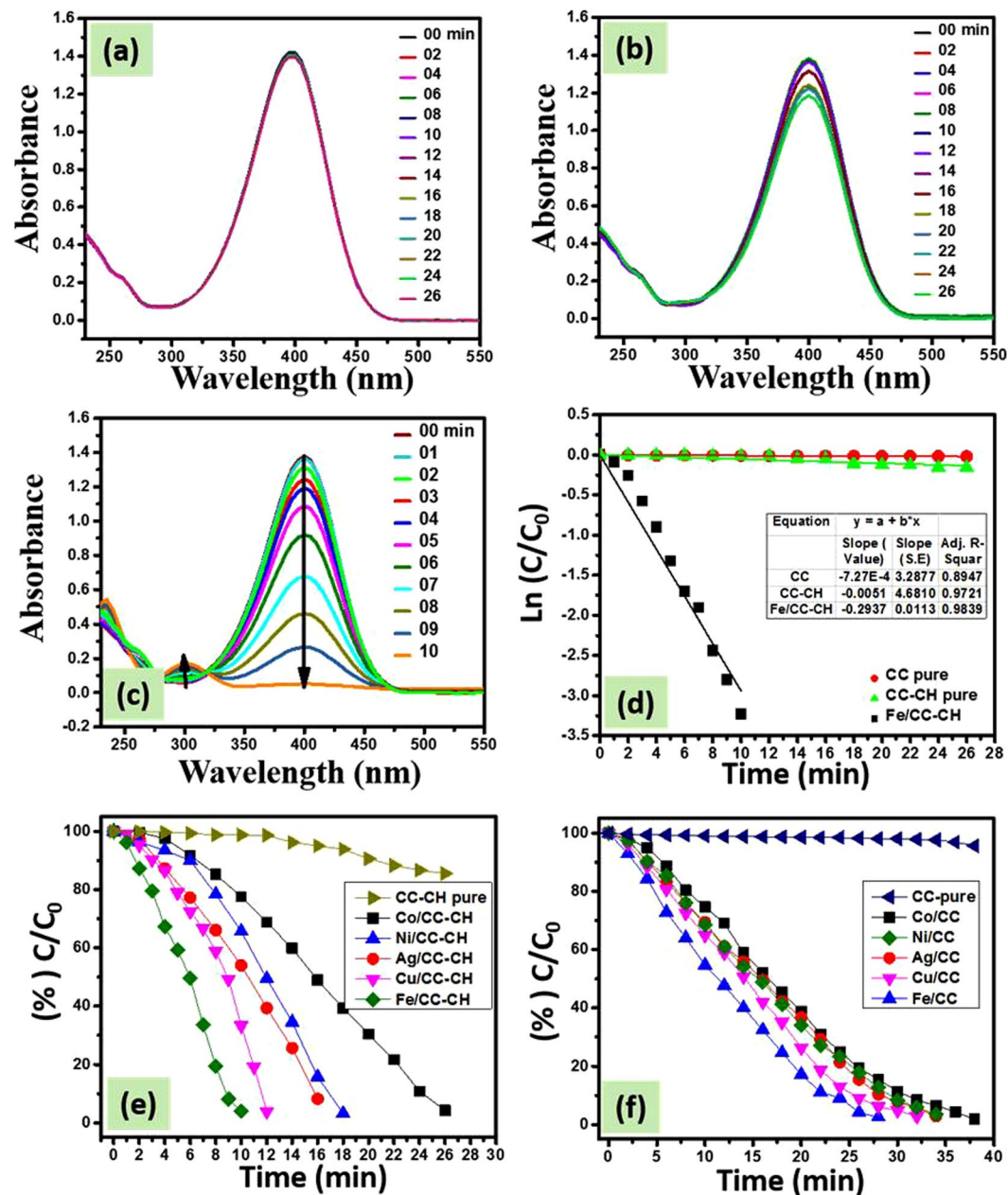


Figure 8. UV-vis spectra of 4-NP reduction as a function of time by NaBH_4 in the presence of bare CC (a), bare CC-CH (b) and Fe/CC-CH (c), $\ln(C/C_0)$ vs time for the reaction occur in the presence of bare CC, CC-CH and Fe/CC-CH (d), percent C/C_0 of 4-NP as a function of time by NaBH_4 in the presence of bare CC-CH and loaded with Fe, Cu, Ag, Ni and Co nanoparticles (e) and bare CC loaded with Fe, Cu, Ag, Ni and Co nanoparticles (f). Experimental conditions: 3 mL of 0.1 mM 4-NP solution, 0.5 mL of 0.1 M NaBH_4 aqueous solution and $0.4 \times 2 \text{ cm}^2$ of the respective catalytic strip.

Catalytic Property. 4-NP transformation to 4-AP. The catalytic activity of the different M^0 template on CC-CH strips was analyzed by using it as a catalyst mainly in two (4-NP and Rh-B) degradation reactions. First, we studied the 4-NP transformation to 4-aminophenol (4-AP) in the presence of prepared catalytic materials. The

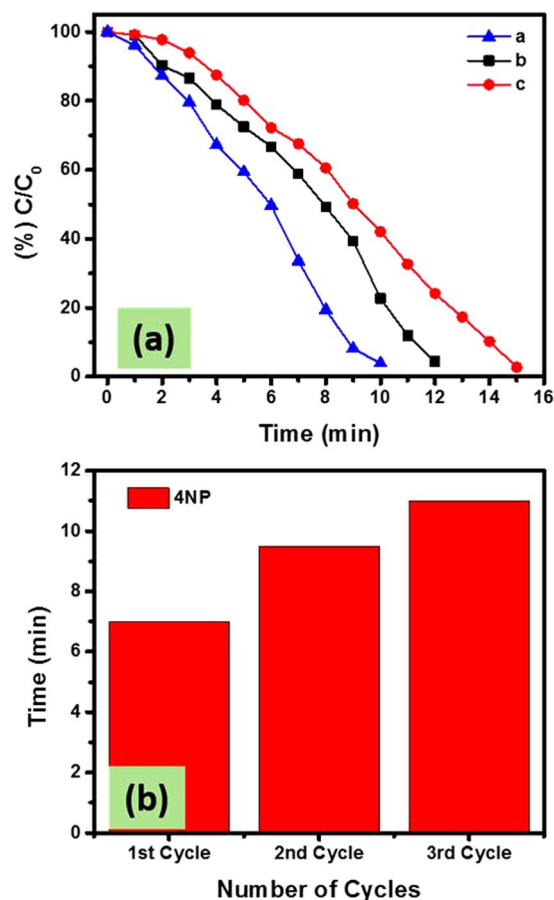


Figure 9. Percent reduction of 4-NP by NaBH₄ in the presence of same catalytic strip Fe/CC-CH re-used three times (a), time taken by recycling catalyst Fe/CC-CH for 70% reduction of 4-NP (b).

catalytic conversion of 4-NP to 4-AP has been extensively studied from the last few years, because it may be an efficient and greener method for the preparation of 4-AP^{50–52}. 4-AP is an efficient intermediate and raw material for the preparation of several medicinal and cosmetic products^{53,54}. Besides, it is reported that 4-AP is less toxic than nitroaromatic compounds and can be easily mineralized and removed from the environment^{55,56}. Therefore, catalytic conversion of 4-NP to 4-AP is an efficient process and when analysis of catalytic activity of catalyst is required this reaction is often chosen as a model reaction.

A CC strip of dimension $0.4 \times 2 \text{ cm}^2$ was introduced in UV cuvette containing 3 mL of 4-NP aqueous solution and 0.5 mL of NaBH₄. No change in color of the solution was observed. Moreover, by analyzing UV-visible spectral data before and after 26 min insertion of CC, a slight decrease in the intensity was observed at 400 nm (main broad peak) (Fig. 8a). Similarly, the incorporation of CC-CH, slightly changes the color of 4-NP and its UV-visible spectra (Fig. 8b). Such a slight decrease in intensity might be due to the physical adsorption of 4-NP by CC or CH, which also indicates that pure CC and CC-CH have no catalytic property. Contrary to bare CC and CC-CH strips, when M⁰ loaded strips were introduced to the reaction matrix of same conditions, the disappearance of color of the solution was observed as shown in Fig. SI 1. The intensity of the peak at 400 nm was gradually disappeared and completely vanished after 10, 12, 16, 18 and 26 min, respectively in the presence of CC-CH loaded with zero-valent Fe, Cu, Ag, Ni and Co nanoparticles (Fig. 8c and Fig. SI 2a–d). In this catalytic reduction reaction of 4-NP, the resulted increase in a new absorption band at 300 nm is recognized as the formation of 4-AP. Probably, the mechanism of this reaction remains the topic of discussion because it may involve complicated intermediates located on the surface of the NPs^{57,58}. However, the isosbestic point approximately at wavelength of 320 nm exhibits the complete conversion 4-NP to 4-AP without side reaction^{58,59}. The CC loaded with Fe, Cu, Ag, Ni and Co nanoparticles took 28, 32, 34, 34 and 38 min for complete reduction of 4-NP aqueous solution (Fig. 8f). In comparison of percent remaining concentration (%C_t/C₀) of nitrophenol versus time in the presence of CC and CC-CH loaded with different M⁰, it can be observed that Fe/CC-CH exhibited good catalytic efficiency (Fig. 8d and f), which suggests that Fe-NPs are more active towards nitrophenols reduction. These results strongly support the superior and excellent catalytic activity of the Fe nanoparticles template in thin CH layers over CC. A small induction period can be revealed over all catalytic strips. Generally, it is considered that the induction period is due to the diffusion of 4-nitrophenolate ions onto the surface of catalyst to be adsorbed prior to the start of the reaction⁶⁰.

The 4-NP reductive conversion to 4-AP in the presence of strong reducing agent NaBH₄, is six electron conversion process^{32,50}. The conversion of 4-NP to 4-AP is thermodynamically favorable in the presence of NaBH₄,

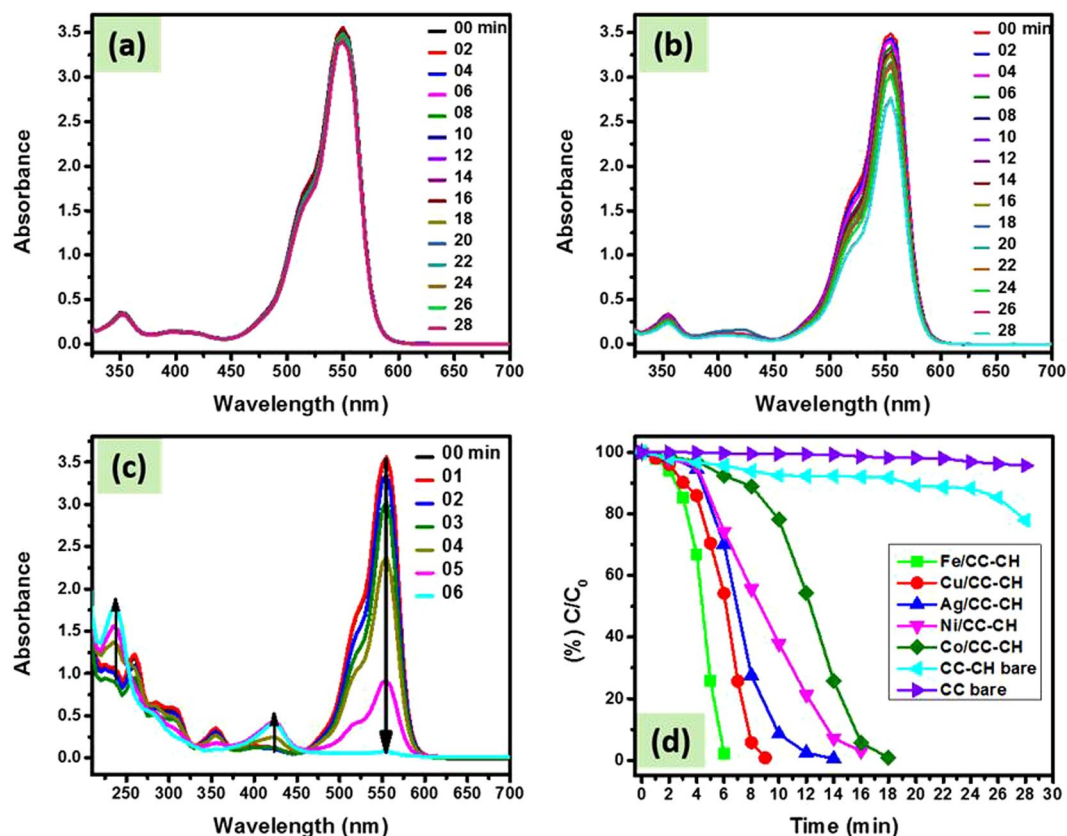


Figure 10. UV-vis spectra of Rh-B reduction as a function of time by NaBH_4 in the presence of bare CC (a), bare CC-CH (b), Fe/CC-CH (c) and percent C/C_0 of Rh-B as a function of time by NaBH_4 in the presence of bare CC, bare CC-CH and CC-CH loaded with Fe, Cu, Ag, Ni and Co nanoparticles (d). Experimental conditions: 3 mL of 0.05 mM Rh-B solution, 0.5 mL of 0.1 M NaBH_4 aqueous solution and $0.4 \times 2 \text{ cm}^2$ of the respective catalytic strip.

because their standard electrode potential is greater than zero, *i.e.* 0.67 V^{32,61}. However, this conversion reaction is kinetically unfavorable in the absence of suitable and efficient catalyst as evidenced experimentally by the use of CC and CC-CH strips. The kinetic barrier can be bypassed through the placement of suitable catalyst like in the present case demonstrated as supported MNPs. It was previously demonstrated that introduction of NaBH_4 in nitrophenols produce nitrophenolate ions, the borohydrides ions (BH_4^-) and nitrophenolate ions get adsorbed on the surface of the catalyst for transfer of electrons. Most of the time, these reduction reactions proceed with *pseudo-first-order* kinetics, provided that NaBH_4 is used in excess amount^{32,60}. The natural log of absorbance ratios ($\ln(C/C_0)$) of the peak at 400 nm was plotted against time for 4-NP aqueous solution (Fig. 8d), where CC, CC-CH and Fe/CC-CH were used as a catalyst. All the data in the figure of $\ln(C/C_0)$ vs time followed linear equation, which suggests that the reaction progressed with *pseudo-first-order* kinetics. The rates of reaction were 0.0007, 0.0051 and 0.2937 min^{-1} for CC, CC-CH and Fe/CC-CH.

Although metal nanoparticles were reported as an effective catalyst for the conversion of 4-NP to 4-AP, but they are difficult to separate from reaction matrix and to re-use for next cycle. Therefore, for reusability purpose the preparation of easy separable catalyst is rather essential. The $M^0/\text{CC-CH}$ catalytic strip can be easily pulled out from the reaction matrix. After one time use of the catalytic strip of Fe/CC-CH in 4-NP to 4-AP reaction, the same strip was washed with DI water and used in new reaction of 4-NP. The plot of (% C/C_0) as function of time, while using the same strip of Fe/CC-CH for 4-NP reduction is manifested in Fig. 9a. It can be observed that more than 95% of 4-NP was transformed into 4-AP during three time use of the same catalytic strip. The time taken by re-using the same catalytic strip of Fe/CC-CH for 70% reduction of 4-NP can be seen from Fig. 9b. The increase in reduction time was observed using the same catalytic strip, which indicated the diminution in catalytic performance. Such a decrease in the catalytic performance might be due to the oxidation of Fe nanoparticles during handling and their slight release to the solution matrix.

Rhodamine-B reduction. Same procedure was applied for Rh-B reduction as applied for 4-NP. Rh-B is one of the important xanthene dye and famous for its stability, which is widely utilized as a colorant in textiles and food stuffs^{62,63}. It is harmful to human beings and causes irritation of the eyes, skin and respiratory tract. The reproductive and developmental toxicity, carcinogenicity, chronic toxicity and neurotoxicity have been experimentally proven toward humans and animals^{64,65}. Keeping the harmful effects and hazardous nature of Rh-B in view, many

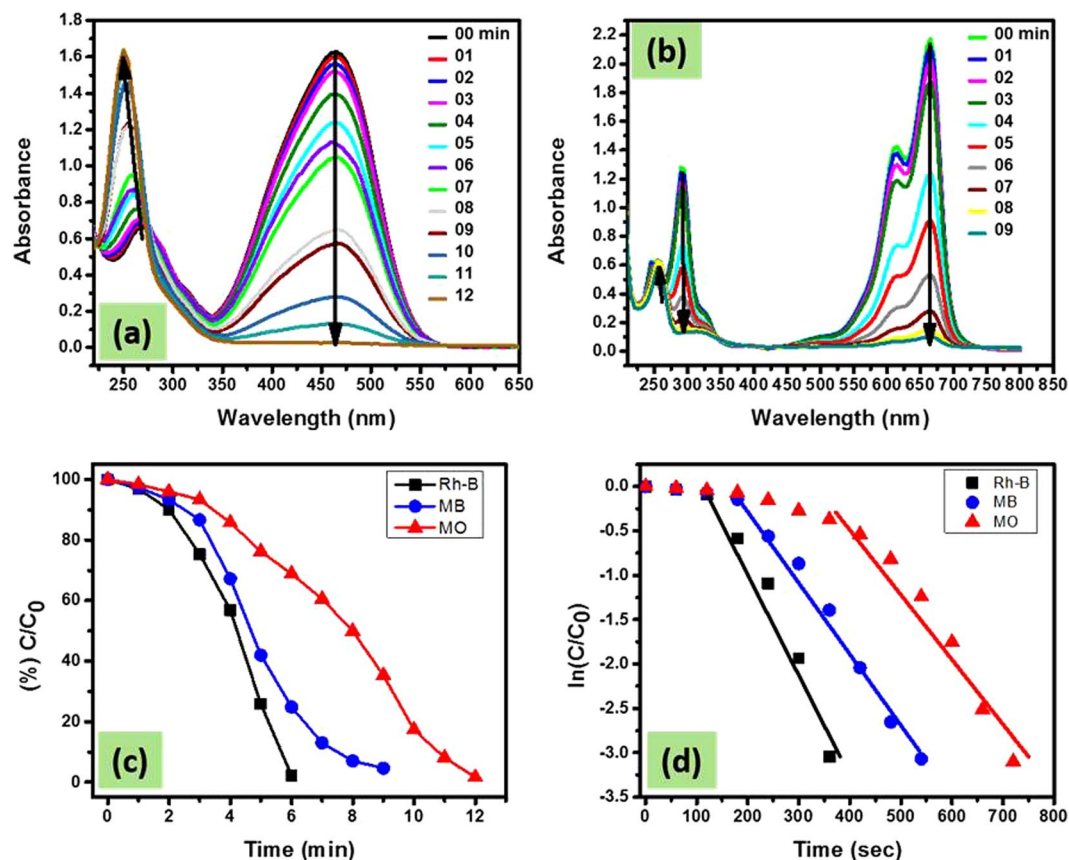


Figure 11. UV-vis spectra of MO (a) and MB (b) reduction as a function of time by NaBH_4 in the presence of Fe/CC-CH catalytic strip, Percent C/C_0 vs time for Rh-B, MO and MB (c), and and their $\ln(C/C_0)$ values as a function of time (d) Experimental conditions: 3 mL of 0.05 mM Rh-B or MO or MB solution with 0.5 mL of 0.1 M NaBH_4 aqueous solution and $0.4 \times 2 \text{ cm}^2$ of the respective catalytic strip.

efforts were made to degrade it from aqueous environment^{66–68}. The UV-vis spectra of reduction of Rh-B as function of time are manifested in Fig. 10a–c and Fig. SI 3a–d. As was expected, a slight decrease was observed in the intensity at 552 nm for the bare CC and CC-CH in 28 min (Fig. 10a,b). Besides, the CC-CH loaded with M^0 show catalytic efficiency toward Rh-B. The time taken for complete reduction of Rh-B was 18, 16 and 14 min in presence of CC-CH loaded with Co, Ni and Ag nanoparticles, while it took 9 and 6 min for Cu and Fe nanoparticles respectively. Inducing period existed in the presence of all catalyst for reduction reaction of Rh-B by NaBH_4 . However, the inducing periods were not identical, which show the difference in catalytic approach by different metal nanoparticles. The remaining percent of Rh-B was plotted against time in presence of various MNPs templated on CC-CH (Fig. 10d). It can be observed that Fe/CC-CH strip has high catalytic efficiency as compared to other loaded nanoparticles, which show the superior catalytic activity of Fe^0 nanoparticles towards Rh-B.

MO and MB reduction. Beside Rh-B dye, we also investigated the catalytic affinity of Fe/CC-CH on other organic dyes like MO and MB in the above NaBH_4 system. In the UV-vis absorption spectra of these dyes, the highest absorption peaks were observed at 464 for MO and 664 for MB. After adding NaBH_4 solution in the cuvette containing dyes solution, the site of the absorption peak and intensity did not change, implying that between dyes and NaBH_4 no reductive reaction took place. However, the peak intensities gradually decreased with time by introducing Fe/CC-CH strip to the above dye- NaBH_4 system (Fig. 11a,b). Similar to the reduction of Rh-B, these dyes reduction was at slower rate in the start of the reaction called as incubation/inducing period. Obviously, the different change trend under the same reaction conditions should originate from difference in molecular structure of the dyes. In general, the electron transfer from the BH_4^- ions onto the dyes molecules are responsible for the reduction of dyes, which take place with assistance of catalyst (here Fe/CC-CH)^{69,70}. The overall process can be explained with electron relay system. The catalytic reduction started by Fe nanoparticles by transmitting electrons from the donor NaBH_4 to the dye molecule. Actually, when NaBH_4 was added to the reaction matrix, the Fe nanoparticles may be trapped by the hydride from BH_4^- ions and adsorbed on the surface of Fe/CC-CH strip and transfer its electron to the Fe nanoparticles. After the electron transfer to the Fe nanoparticles from BH_4^- ions the hydrogen atom formed, which subsequently attack a nearby dye molecule. Then spontaneously hydrogenation of the dye occurs by the transfer of these electrons to dye molecule. In other words, a negatively charged Fe nanoparticles (having excess of electrons), finally released electrons to an electron

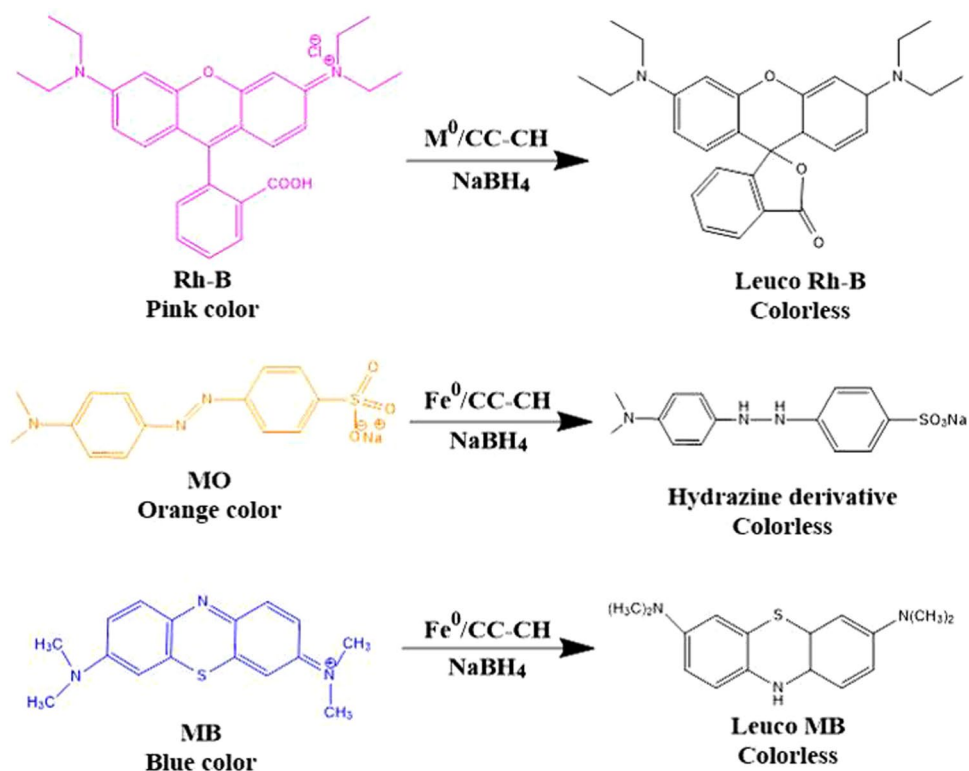


Figure 12. Reduction reactions of dyes to their leuco forms (hydrazine derivative of MO).

Catalysts	Reduction reaction of	K_{app} (min^{-1})	References
Fe/CC-CH	4-NP	0.2937	This work
Cu/ZnPc-CH	4-NP	0.0513	25
Au/CA	4-NP	0.14–0.20	52
Ag/CB-CH	4-NP	0.1040	26
Ag/CH-FP	4-NP	0.2340	60
Au (10)/TiO ₂	4-NP	0.17	75
FeNi ₂ alloy nanostructure	4-NP	0.06	76
Fe/CC-CH	Rh-B	0.3804	This work
Bi ₂ WO ₆	Rh-B	0.0517	77
Fe/CC-CH	MO	0.1698	This work
Ni/CH-FP	MO	0.116	32
Fe/CC-CH	MB	0.2802	This work
Ag/RGO	MB	0.014	78

Table 2. Comparison of catalysts for the reduction of 4-NP and azo dyes with literature.

acceptor (here dye molecule), producing their reduced form (leuco Rh-B, leuco MB and hydrazine derivate for MO) as shown by the appearance of the new peaks around 250 nm in their time dependent UV-absorption spectra (Figs 10c, 11a, b and 12). The cationic dyes (Rh-B and MB) reduced first followed by anionic dye MO. The nature of a dye (*via.*, charge, presence of S/N donor atoms, hydrophobicity) may affect its rate of reduction^{71,72}. In general, cationic dyes like Rh-B and MB have a high catalytic reaction rate then anionic dyes like MO, because of electrostatic interactions. It is clear that upon introduction of Fe/CC-CH catalytic strip in various dyes solution, the reduction reaction completed about 6, 9 and 12 min for RB, MB and MO, respectively. These suggests that Fe/CC-CH is responsible for the possible cleavage of -N=N- double bond in azo dye structure and thus decolorizing the solutions⁷³. Also, the appearance of new peaks in the UV-vis absorption spectra indicated the formation of new products. From Fig. 11c, it can be clearly observed that Fe/CC-CH has high catalytic efficiency of reduction towards Rh-B. More detailed information was deduced from the kinetics of reduction reactions. In these experiments, the concentration of NaBH_4 was much higher than dyes and could be consider as constant during the reaction kinetics. The order of the reaction was determined by *pseudo first order* kinetic equation, $\ln(C/C_0) = -kt$. The

values of $\ln(C/C_0)$ versus time was plotted as shown in Fig. 11d. The values in the presence of Fe/CC-CH, didn't follow fully linearity of the equation might be due to the inducing period in the start of the reaction and also the bubble formation in the cuvette during the reaction. The rate of reactions calculated after deducing the inducing periods were 0.00283, 0.00467 and 0.00634 sec^{-1} for MO, MB and Rh-B, respectively. The high rate constant value deduced the high catalytic nature of Fe/CC-CH strip toward Rh-B, which is much higher than the reported literatures^{71,74}. Comparison of our work with literature for the reduction of 4-NP and azo dyes is manifested in Table 2.

Conclusion

In summary, we present a simple method for the preparation of MNPs in the CH coating layer over cotton cloth for catalytic purpose. FTIR, XRD, XPS and TGA analysis confirmed that other properties of the cellulose fibers and CH did not change during the process. FESEM and EDX analysis exposed that the Fe nanoparticles were synthesized on CC-CH strips. Bare CC and CC-CH loaded with different MNPs were investigated for catalytic reduction of 4-NP and Rh-B by NaBH_4 . We showed that Fe/CC-CH strips have good catalytic activity for 4-NP and Rh-B as well as for MO and MB dyes reduction. The reduction reaction for 4-NP, Rh-B, MO and MB by NaBH_4 in presence of Fe/CC-CH strip were accomplished within 10, 6, 12 and 9 min, respectively. The Fe/CC-CH was re-used for three time in the reduction reaction of 4-NP, where more than 90% reduction was achieved in 15 min. The separation of the catalytic strip was nicely done by simply pulling the strip from the reaction matrix.

References

- Fihri, A., Bouhrara, M., Nekoueishahraki, B., Basset, J.-M. & Polshettiwar, V. Nanocatalysts for Suzuki cross-coupling reactions. *Chemical Society Reviews* **40**, 5181–5203 (2011).
- Caliskan, S., Zahmakıran, M., Durap, F. & Özkar, S. Hydrogen liberation from the hydrolytic dehydrogenation of dimethylamine–borane at room temperature by using a novel ruthenium nanocatalyst. *Dalton Transactions* **41**, 4976–4984 (2012).
- Zhang, Q., Deng, W. & Wang, Y. Effect of size of catalytically active phases in the dehydrogenation of alcohols and the challenging selective oxidation of hydrocarbons. *Chemical Communications* **47**, 9275–9292 (2011).
- Baig, R. N., Verma, S., Varma, R. S. & Nadagouda, M. N. Magnetic Fe@ g-C₃N₄: a photoactive catalyst for the hydrogenation of alkenes and alkynes. *ACS Sustainable Chemistry & Engineering* **4**, 1661–1664 (2016).
- Sarkar, B., Pendem, C., Konathala, L. S., Sasaki, T. & Bal, R. Pt nanoparticle supported on nanocrystalline CeO₂: highly selective catalyst for upgradation of phenolic derivatives present in bio-oil. *Journal of Materials Chemistry A* **2**, 18398–18404 (2014).
- Shen, J., Yin, X., Karpuzov, D. & Semagina, N. PVP-stabilized mono- and bimetallic Ru nanoparticles for selective ring opening. *Catalysis Science & Technology* **3**, 208–221 (2013).
- Kamal, T., Khan, S. B. & Asiri, A. M. Synthesis of zero-valent Cu nanoparticles in the chitosan coating layer on cellulose microfibers: evaluation of azo dyes catalytic reduction. *Cellulose* **23**, 1911–1923 (2016).
- Yazdian, F., Rasekh, B., Rashedi, H. & Rostami, A. D. Effect of Metal Nanoparticles on Biological Denitrification Process: A review. *Journal of Applied Biotechnology Reports* **3**, 353–358 (2016).
- Datta, K. *et al.* Micro-mesoporous iron oxides with record efficiency for the decomposition of hydrogen peroxide: morphology driven catalysis for the degradation of organic contaminants. *Journal of Materials Chemistry A* **4**, 596–604 (2016).
- Kaegi, R. *et al.* Behavior of metallic silver nanoparticles in a pilot wastewater treatment plant. *Environmental science & technology* **45**, 3902–3908 (2011).
- Sharma, V. K., Zboril, R. & Varma, R. S. Ferrates: greener oxidants with multimodal action in water treatment technologies. *Accounts of chemical research* **48**, 182–191 (2015).
- Zahmakıran, M. & Özkar, S. Metal nanoparticles in liquid phase catalysis; from recent advances to future goals. *Nanoscale* **3**, 3462–3481 (2011).
- Carino, E. V., Knecht, M. R. & Crooks, R. M. Quantitative analysis of the stability of Pd dendrimer-encapsulated nanoparticles. *Langmuir* **25**, 10279–10284 (2009).
- Yan, W., Chen, B., Mahurin, S. M., Dai, S. & Overbury, S. H. Brookite-supported highly stable gold catalytic system for CO oxidation. *Chemical Communications* 1918–1919 (2004).
- Baig, R. N. & Varma, R. S. Magnetically retrievable catalysts for organic synthesis. *Chemical Communications* **49**, 752–770 (2013).
- Hu, L. *et al.* Stretchable, porous, and conductive energy textiles. *Nano letters* **10**, 708–714 (2010).
- Lewin, M. & Pearce, E. M. *Handbook of Fiber Chemistry, Revised and Expanded*. (Crc press, 1998).
- Liu, W.-W., Yan, X.-B., Lang, J.-W., Peng, C. & Xue, Q.-J. Flexible and conductive nanocomposite electrode based on graphene sheets and cotton cloth for supercapacitor. *Journal of Materials Chemistry* **22**, 17245–17253 (2012).
- Wang, X., Du, Y. & Liu, H. Preparation, characterization and antimicrobial activity of chitosan–Zn complex. *Carbohydrate polymers* **56**, 21–26 (2004).
- O'Callaghan, K. A. & Kerry, J. P. Preparation of low- and medium-molecular weight chitosan nanoparticles and their antimicrobial evaluation against a panel of microorganisms, including cheese-derived cultures. *Food Control* **69**, 256–261 (2016).
- Pang, Y. *et al.* Biodegradable and biocompatible high elastic chitosan scaffold is cell-friendly both *in vitro* and *in vivo*. *Oncotarget* (2017).
- Kumar, M. N. R. A review of chitin and chitosan applications. *Reactive and functional polymers* **46**, 1–27 (2000).
- Ali Khan, S., Bahadar Khan, S., Kamal, T., M Asiri, A. & Akhtar, K. Recent development of chitosan nanocomposites for environmental applications. *Recent patents on nanotechnology* **10**, 181–188 (2016).
- Sakthivel, B. & Dhakshinamoorthy, A. Chitosan as a reusable solid base catalyst for Knoevenagel condensation reaction. *Journal of Colloid and Interface Science* **485**, 75–80 (2017).
- Ali, F. *et al.* Anti-bacterial chitosan/zinc phthalocyanine fibers supported metallic and bimetallic nanoparticles for the removal of organic pollutants. *Carbohydrate Polymers* (2017).
- Ali, F. *et al.* Bactericidal and catalytic performance of green nanocomposite based-on chitosan/carbon black fiber supported monometallic and bimetallic nanoparticles. *Chemosphere* (2017).
- Baig, R. N., Vaddula, B. R., Gonzalez, M. A. & Varma, R. S. N-Allylation of amines with allyl acetates using chitosan-immobilized palladium. *RSC Advances* **4**, 9103–9106 (2014).
- Sahiner, N. Soft and flexible hydrogel templates of different sizes and various functionalities for metal nanoparticle preparation and their use in catalysis. *Progress in Polymer Science* **38**, 1329–1356 (2013).
- Khan, S. B. *et al.* CuO embedded chitosan spheres as antibacterial adsorbent for dyes. *International journal of biological macromolecules* **88**, 113–119 (2016).
- Sahiner, N., Ozay, H., Ozay, O. & Aktas, N. A soft hydrogel reactor for cobalt nanoparticle preparation and use in the reduction of nitrophenols. *Applied Catalysis B: Environmental* **101**, 137–143 (2010).
- Sahiner, N., Ozay, O., Inger, E. & Aktas, N. Superabsorbent hydrogels for cobalt nanoparticle synthesis and hydrogen production from hydrolysis of sodium boron hydride. *Applied Catalysis B: Environmental* **102**, 201–206 (2011).

32. Kamal, T., Khan, S. B. & Asiri, A. M. Nickel nanoparticles-chitosan composite coated cellulose filter paper: an efficient and easily recoverable dip-catalyst for pollutants degradation. *Environmental Pollution* **218**, 625–633 (2016).
33. Hudson, R., Rivière, A., Cirtiu, C. M., Luska, K. L. & Moores, A. Iron-iron oxide core-shell nanoparticles are active and magnetically recyclable olefin and alkyne hydrogenation catalysts in protic and aqueous media. *Chemical Communications* **48**, 3360–3362 (2012).
34. Smuleac, V., Varma, R., Sikdar, S. & Bhattacharyya, D. Green synthesis of Fe and Fe/Pd bimetallic nanoparticles in membranes for reductive degradation of chlorinated organics. *Journal of membrane science* **379**, 131–137 (2011).
35. Kim, J. *et al.* The role of metallic Fe and carbon matrix in Fe₂O₃/Fe/carbon nanocomposite for lithium-ion batteries. *Journal of The Electrochemical Society* **157**, A412–A417 (2010).
36. Heidarpour, F. *et al.* Nano silver-coated polypropylene water filter: I. Manufacture by electron beam gun using a modified balzers 760 machine. *Dig. J. Nanomater. Biostruct* **5**, 787–796 (2010).
37. Faghihi, K. & Shabaniyan, M. Thermal and optical properties of silver-polyimide nanocomposite based on diphenyl sulfone moieties in the main chain. *Journal of the Chilean Chemical Society* **56**, 665–667 (2011).
38. Barakat, N. A. *et al.* Cobalt nanofibers encapsulated in a graphite shell by an electrospinning process. *Journal of Materials Chemistry* **19**, 7371–7378 (2009).
39. Abidi, N., Cabrales, L. & Haigler, C. H. Changes in the cell wall and cellulose content of developing cotton fibers investigated by FTIR spectroscopy. *Carbohydrate Polymers* **100**, 9–16 (2014).
40. Oh, S. Y., Yoo, D. I., Shin, Y. & Seo, G. FTIR analysis of cellulose treated with sodium hydroxide and carbon dioxide. *Carbohydrate Research* **340**, 417–428 (2005).
41. Gregorio-Jauregui, K. M. *et al.* One-step method for preparation of magnetic nanoparticles coated with chitosan. *Journal of Nanomaterials* **2012**, 4 (2012).
42. Kumar, P. *et al.* Novel high-viscosity polyacrylamidated chitosan for neural tissue engineering: fabrication of anisotropic neurodurable scaffold via molecular disposition of persulfate-mediated polymer slicing and complexation. *International journal of molecular sciences* **13**, 13966–13984 (2012).
43. Tan, B. J., Klabunde, K. J. & Sherwood, P. M. XPS studies of solvated metal atom dispersed (SMAD) catalysts. Evidence for layered cobalt-manganese particles on alumina and silica. *Journal of the American Chemical Society* **113**, 855–861 (1991).
44. McIntyre, N. & Cook, M. X-ray photoelectron studies on some oxides and hydroxides of cobalt, nickel, and copper. *Analytical chemistry* **47**, 2208–2213 (1975).
45. Üzümlü, Ç. *et al.* Application of zero-valent iron nanoparticles for the removal of aqueous Co²⁺ ions under various experimental conditions. *Chemical Engineering Journal* **144**, 213–220 (2008).
46. Liu, A., Liu, J., Pan, B. & Zhang, W.-X. Formation of lepidocrocite (γ -FeOOH) from oxidation of nanoscale zero-valent iron (nZVI) in oxygenated water. *RSC Advances* **4**, 57377–57382 (2014).
47. Li, X.-Q. & Zhang, W.-X. Sequestration of metal cations with zerovalent iron nanoparticles a study with high resolution X-ray photoelectron spectroscopy (HR-XPS). *The Journal of Physical Chemistry C* **111**, 6939–6946 (2007).
48. Khan, S. B. *et al.* Assessment of antibacterial cellulose nanocomposites for water permeability and salt rejection. *Journal of Industrial and Engineering Chemistry* **24**, 266–275 (2015).
49. Kim, D. *et al.* UV-cured poly (urethane acrylate) composite films containing surface-modified tetrapod ZnO whiskers. *Composites Science and Technology* **75**, 84–92 (2013).
50. Bae, S., Gim, S., Kim, H. & Hanna, K. Effect of NaBH₄ on properties of nanoscale zero-valent iron and its catalytic activity for reduction of p-nitrophenol. *Applied Catalysis B: Environmental* **182**, 541–549 (2016).
51. Pandey, S. & Mishra, S. B. Catalytic reduction of p-nitrophenol by using platinum nanoparticles stabilised by guar gum. *Carbohydrate polymers* **113**, 525–531 (2014).
52. Saha, S., Pal, A., Kundu, S., Basu, S. & Pal, T. Photochemical green synthesis of calcium-alginate-stabilized Ag and Au nanoparticles and their catalytic application to 4-nitrophenol reduction. *Langmuir* **26**, 2885–2893 (2009).
53. Khosroshahi, A. M., Aflaki, F., Saemiyani, N., Abdollahpour, A. & Asgharian, R. Simultaneous determination of paracetamol, 4-Aminophenol, 4-Chloroacetanilid, Benzyl alcohol, Benzaldehyde and EDTA by HPLC method in paracetamol injection ampoule. *Journal of Pharmaceutical and Health Sciences* **4**, 61–69 (2016).
54. Pavkovic, M. *et al.* Detection of drug-induced acute kidney injury in humans using urinary KIM-1, miR-21, -200c and -423. *Toxicological Sciences*, kfw077 (2016).
55. Guo, P. *et al.* Catalytic reduction-adsorption for removal of p-nitrophenol and its conversion p-aminophenol from water by gold nanoparticles supported on oxidized mesoporous carbon. *Journal of colloid and interface science* **469**, 78–85 (2016).
56. Hussain, M. M., Rahman, M. M. & Asiri, A. M. Ultrasensitive and selective 4-aminophenol chemical sensor development based on nickel oxide nanoparticles decorated carbon nanotube nanocomposites for green environment. *Journal of Environmental Sciences* (2016).
57. Corma, A., Concepción, P. & Serna, P. A different reaction pathway for the reduction of aromatic nitro compounds on gold catalysts. *Angewandte Chemie* **119**, 7404–7407 (2007).
58. Nasrollahzadeh, M., Sajadi, S. M. & Dasmeh, H. R. *In situ* green synthesis of Cu nanoparticles supported on natural Natrolite zeolite for the reduction of 4-nitrophenol, congo red and methylene blue. *IET Nanobiotechnology* (2016).
59. Pradhan, N., Pal, A. & Pal, T. Silver nanoparticle catalyzed reduction of aromatic nitro compounds. *Colloids and Surfaces A: Physicochemical and Engineering Aspects* **196**, 247–257 (2002).
60. Ahmad, I., Kamal, T., Khan, S. B. & Asiri, A. M. An efficient and easily retrievable dip catalyst based on silver nanoparticles/chitosan-coated cellulose filter paper. *Cellulose* **1–12** (2016).
61. Ahmad, I., Kamal, T., Khan, S. B. & Asiri, A. M. An efficient and easily retrievable dip catalyst based on silver nanoparticles/chitosan-coated cellulose filter paper. *Cellulose* **23**, 3577–3588 (2016).
62. Richardson, S. D., Willson, C. S. & Rusch, K. A. Use of rhodamine water tracer in the marshland upwelling system. *Groundwater* **42**, 678–688 (2004).
63. Mehrdad, A., Massoumi, B. & Hashemzadeh, R. Kinetic study of degradation of Rhodamine B in the presence of hydrogen peroxide and some metal oxide. *Chemical engineering journal* **168**, 1073–1078 (2011).
64. Kornbrust, D. & Barfknecht, T. Testing of 24 food, drug, cosmetic, and fabric dyes in the *in vitro* and the *in vivo/in vitro* rat hepatocyte primary culture DNA repair assays. *Environmental and Molecular Mutagenesis* **7**, 101–120 (1985).
65. Soni, H., Kumar, J. N., Patel, K. & Kumar, R. N. Photo-catalytic decoloration of Rhodamine B dye using ZVI nanopowder synthesized by chemical reduction method. *Indian Journal of Nanoscience* **3**, 2 (2015).
66. Jeyapragasam, T. & Kannan, R. S. Microwave assisted green synthesis of silver nanorods as catalysts for rhodamine B degradation. *Russian Journal of Physical Chemistry A* **90**, 1334–1337 (2016).
67. Mishra, K., Poudel, T. N., Basavegowda, N. & Lee, Y. R. Enhanced catalytic performance of magnetic Fe₃O₄-MnO₂ nanocomposites for the decolorization of rhodamine B, reduction of 4-nitroaniline, and sp³ C-H functionalization of 2-methylpyridines to isatins. *Journal of Catalysis* **344**, 273–285 (2016).
68. Du, S., Liao, Z., Qin, Z., Zuo, F. & Li, X. Polydopamine microparticles as redox mediators for catalytic reduction of methylene blue and rhodamine B. *Catalysis Communications* **72**, 86–90 (2015).
69. Kundu, S., Mukadam, M., Yusuf, S. & Jayachandran, M. Formation of shape-selective magnetic cobalt oxide nanowires: environmental application in catalysis studies. *CrystEngComm* **15**, 482–497 (2013).

70. Lu, D., Ni, Y., Wu, H., Wang, M. & Sheng, E. Preparation and catalytic properties of porous CoP nanoflakes via a low-temperature phosphidation route. *CrystEngComm* **18**, 5580–5587 (2016).
71. Lijuan, S. *et al.* Recyclable Fe₃O₄@SiO₂-Ag magnetic nanospheres for the rapid decolorizing of dye pollutants. *Chinese Journal of Catalysis* **34**, 1378–1385 (2013).
72. Jana, N. R. & Pal, T. Redox catalytic property of still-growing and final palladium particles: a comparative study. *Langmuir* **15**, 3458–3463 (1999).
73. Aljamali, N. M. Review in azo compounds and its biological activity. *Biochemistry and Analytical Biochemistry* **4**, 1 (2015).
74. Féral-Martin, C., Birot, M., Deleuze, H., Desforges, A. & Backov, R. Integrative chemistry toward the first spontaneous generation of gold nanoparticles within macrocellular polyHIPE supports (Au@polyHIPE) and their application to eosin reduction. *Reactive and Functional Polymers* **67**, 1072–1082 (2007).
75. Li, B. *et al.* Synthesis of hierarchically porous metal oxides and Au/TiO₂ nanohybrids for photodegradation of organic dye and catalytic reduction of 4-nitrophenol. *Journal of Catalysis* **329**, 368–378 (2015).
76. Wu, K.-L., Yu, R. & Wei, X.-W. Monodispersed FeNi₂ alloy nanostructures: solvothermal synthesis, magnetic properties and size-dependent catalytic activity. *CrystEngComm* **14**, 7626–7632 (2012).
77. Fu, H., Pan, C., Yao, W. & Zhu, Y. Visible-light-induced degradation of rhodamine B by nanosized Bi₂WO₆. *J. Phys. Chem. B* **109**, 22432–22439 (2005).
78. He, C., Liu, Z., Lu, Y., Huang, L. & Yang, Y. Graphene-supported silver nanoparticles with high activities toward chemical catalytic reduction of Methylene Blue and electrocatalytic oxidation of hydrazine. *International Journal Of Electrochemical Science* **11**, 9566–9574 (2016).

Acknowledgements

The authors are grateful to the Department of Chemistry and the Center of Excellence for Advanced Materials Research at King Abdulaziz University for providing research facilities.

Author Contributions

F.A. performed the experiment and wrote the manuscript, S.B.K. designed the experiment and revised the manuscript while A.M.A., T.K., K.A.A. and T.R.A.S. also revised the manuscript and provided all the materials and instruments. Finally, all the authors revised and approved the manuscript.

Additional Information

Competing Interests: The authors declare that they have no competing interests.

Publisher's note: Springer Nature remains neutral with regard to jurisdictional claims in published maps and institutional affiliations.



Open Access This article is licensed under a Creative Commons Attribution 4.0 International License, which permits use, sharing, adaptation, distribution and reproduction in any medium or format, as long as you give appropriate credit to the original author(s) and the source, provide a link to the Creative Commons license, and indicate if changes were made. The images or other third party material in this article are included in the article's Creative Commons license, unless indicated otherwise in a credit line to the material. If material is not included in the article's Creative Commons license and your intended use is not permitted by statutory regulation or exceeds the permitted use, you will need to obtain permission directly from the copyright holder. To view a copy of this license, visit <http://creativecommons.org/licenses/by/4.0/>.

© The Author(s) 2017